

## Supplementary Information

### The large subunit of the regulatory [NiFe]-hydrogenase from *Ralstonia eutropha* – A minimal hydrogenase?

Giorgio Caserta,<sup>a</sup> Christian Lorent,<sup>a</sup> Alexandre Ciaccafava,<sup>a</sup> Matthias Keck,<sup>b</sup> Raffaella Breglia,<sup>c</sup> Claudio Greco,<sup>c</sup> Christian Limberg,<sup>b</sup> Peter Hildebrandt,<sup>a</sup> Stephen P. Cramer,<sup>d</sup> Ingo Zebger,<sup>a</sup> and Oliver Lenz<sup>a</sup>

<sup>a</sup> Institut für Chemie, Technische Universität Berlin, Straße des 17. Juni 135, 10623 Berlin, Germany

<sup>b</sup> Department of Chemistry, Humboldt-Universität zu Berlin, Brook-Taylor-Straße 2, 12489 Berlin, Germany

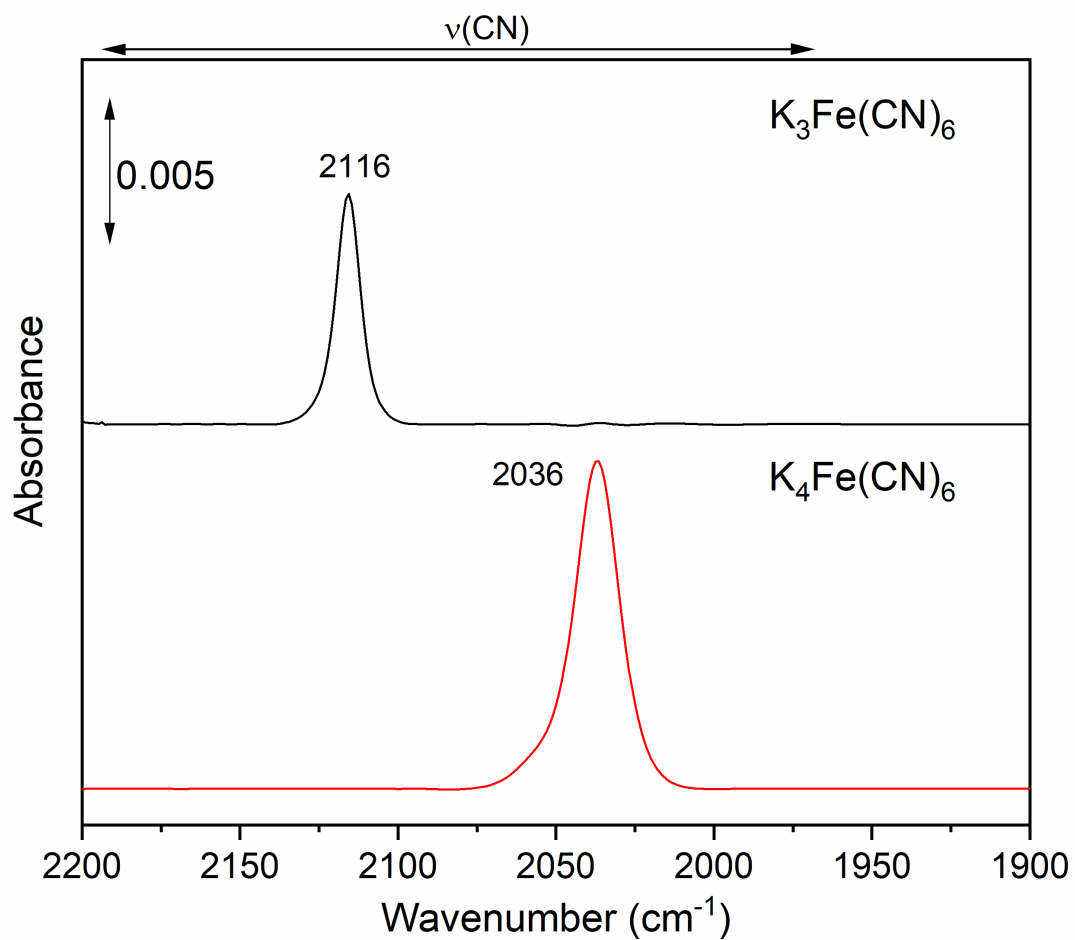
<sup>c</sup> Department of Earth and Environmental Sciences, Milano-Bicocca University, Piazza della Scienza 1, 20126 Milan, Italy

<sup>d</sup> SETI Institute, 189 Bernardo Ave., Mountain View, CA 94043, United States

### Table of Contents

|  |     |
|--|-----|
| <b>Figure S1.</b> $\nu(\text{CN})$ stretching modes of $\text{K}_3\text{Fe}(\text{CN})_6$ and $\text{K}_4\text{Fe}(\text{CN})_6$ | S3  |
| <u>Purification of the large subunit HoxC</u> ; <b>Figures S2, S3</b>  | S4  |
| <b>Table S1.</b> CO and CN stretching modes for the active site redox states   | S6  |
| <b>Figure S4.</b> IR spectra of monomeric and dimeric HoxC species   | S7  |
| <b>Figure S5.</b> IR spectra of oxidatively and reductively treated HoxC   | S8  |
| <u>TDDFT calculations</u> ; <b>Figures S6, S7, S8, S9</b> ; <b>Tables S2, S3, S4</b>   | S9  |
| <b>Figure S10.</b> IR spectra of purified RH   | S15 |
| <b>Figure S11.</b> IR and EPR spectra of $\text{K}_3\text{Fe}(\text{CN})_6$ -oxidized HoxC                                       | S16 |
| <b>Figure S12.</b> IR (second derivatives) and EPR spectra of oxidized RH protein  | S17 |
| <b>Figure S13.</b> Temperature-dependent EPR spectra of oxidized HoxC  | S18 |
| <b>Table S5.</b> EPR-derived g-values for HoxC in different redox states   | S19 |
| <b>Table S6.</b> Mössbauer-derived parameters for RH and HoxC  | S19 |
| <b>Table S7.</b> Comparison of HD and $\text{D}_2$ production rates of different [NiFe]-hydrogenases and isolated large subunits | S19 |
| <b>Figure S14.</b> Mössbauer spectra of $^{57}\text{Fe}$ -labelled HoxC in comparison to simulated spectra                       | S20 |
| <b>Figure S15.</b> Raw-data of HD and $\text{D}_2$ electric response as a function of time                                       | S21 |
| <b>Figure S16.</b> HD and $\text{D}_2$ production as a function of HoxC concentration  | S22 |

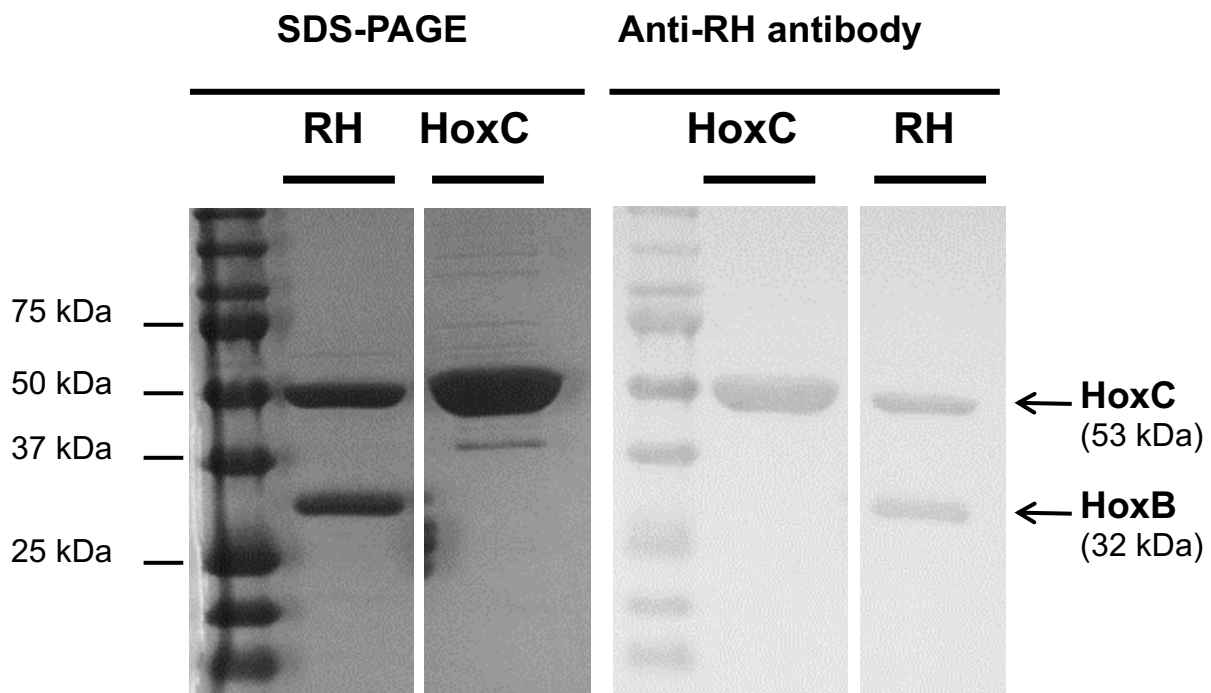
|   |     |
|---|-----|
| <b>Figure S17.</b> Corrected HD ( <b>A</b> ) and D <sub>2</sub> ( <b>B</b> ) currents as a function of H <sub>2</sub> concentration | S23 |
| <b>Figure S18.</b> HD and D <sub>2</sub> current response of monomeric and dimeric HoxC   | S24 |
| <b>Figure S19.</b> HD and D <sub>2</sub> production rates of RH as a function of the pH   | S25 |
| <b>Figure S20.</b> H <sub>2</sub> -dependent methylene blue reduction mediated of HoxC and RH                                       | S26 |
| <b>Table S8.</b> Comparison of HD/D <sub>2</sub> ratios at different HoxC concentrations  | S26 |
| <u>Supplementary References</u>   | S27 |



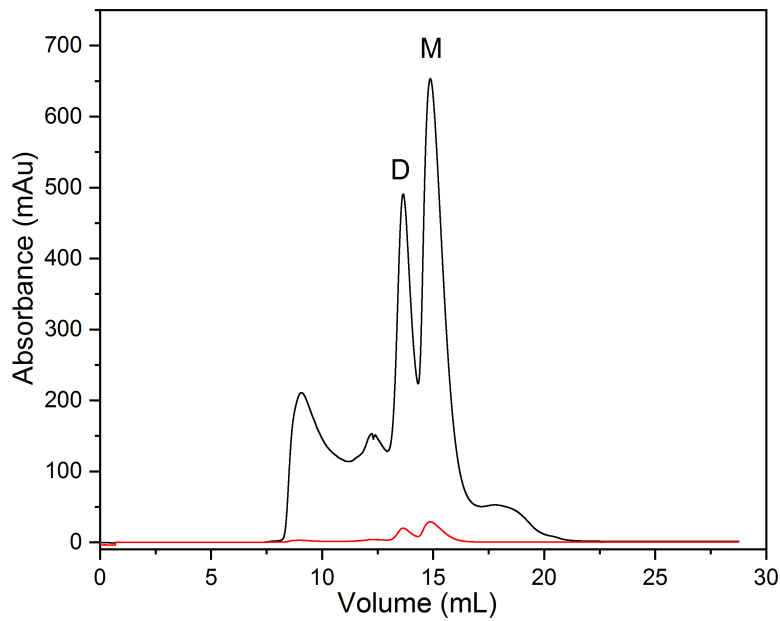
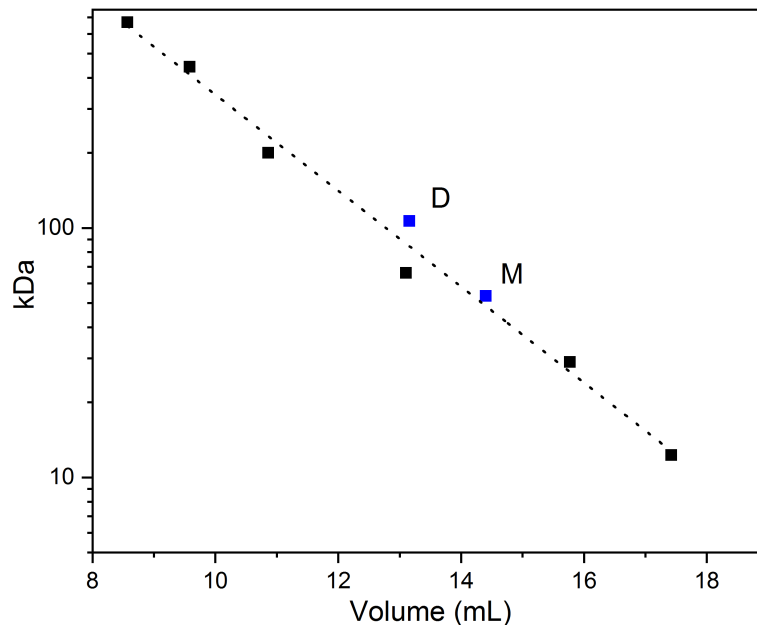
**Figure S1.** IR spectra of 1.0 mM K<sub>3</sub>Fe(CN)<sub>6</sub> and 0.5 mM K<sub>4</sub>Fe(CN)<sub>6</sub> in 50 mM Tris-HCl, with 150 mM NaCl at pH 8.0. The ν(C≡N) stretching mode related to K<sub>3</sub>Fe(CN)<sub>6</sub> is located at 2116 cm<sup>-1</sup>, while K<sub>4</sub>Fe(CN)<sub>6</sub> exhibits a ν(C≡N) stretching mode at 2036 cm<sup>-1</sup>.

## Purification of the large subunit HoxC

For isolation of HoxC we used the previously described strain *R. eutropha* HF574(pGE537), which is deleted for the large subunit genes of the two energy-conserving hydrogenases, MBH and SH, of *R. eutropha* as well as the genes encoding the two subunits, HoxB and HoxC, of the RH. Plasmid pGE537 conferred overexpression of solely *hoxC* equipped with a Strep-tag II-encoding sequence located at the 5' end.<sup>1</sup> An earlier study employing the same strain revealed purified HoxC protein that was incompletely matured resulting in an active site only loaded partially with nickel.<sup>2</sup> Therefore, we adopted a new cultivation protocol as described in the Experimental section. This protocol generally leads to a yield of fully mature hydrogenase proteins caused by the long-term cultivation under microaerobic conditions.<sup>3</sup> N-terminally Strep-tagged HoxC was isolated from the soluble extracts of HF574(pGE537) by using Strep-Tactin-based affinity chromatography. From 13-15 g (wet weight) of cells, we obtained approximately 2 mg of pure, as-isolated HoxC protein (HoxC<sub>ai</sub>). Protein purity and confirmation of the absence of HoxB was demonstrated by SDS-PAGE and corresponding Western blot analysis with antibodies raised against purified RH (Figure S1). Subsequent size-exclusion chromatography afforded the separation of dimeric and monomeric HoxC<sub>ai</sub> preparations (Figure S2). RH protein served as a control and was purified as described previously.<sup>4</sup>



**Figure S2.** SDS-PAGE (left) and Western blot analysis (right) of HoxC (10  $\mu$ g per lane) using antibodies raised against the regulatory hydrogenase (RH, 6  $\mu$ g per lane) from *R. eutropha*.

**A****B**

**Figure S3.** (A) Size exclusion chromatography elution profile of HoxC<sub>ai</sub> on “Superdex S200 Increase 10/300 GL” in 50 mM Tris-HCl with 150 mM NaCl at pH 8.0. The absorbance at 280 nm is depicted in black while the absorbance of the [NiFe] cofactor at 370 nm is depicted in red. (B) Calibration curve on “Superdex S200 Increase 10/300 GL” in 50 mM Tris-HCl at pH 8.0 with 150 mM NaCl is displayed in forms of black squares using Thyroglobulin (670 kDa, 8.57 mL), Apoferritin (443 kDa, 9.58 ml),  $\beta$ -Amylase (200 kDa, 10.86 ml), Bovine serum albumin (66 kDa, 13.1 ml), Carbonic anhydrase (29 kDa, 15.77 ml) and cytochrome C (12.3 kDa, 17.42 ml) as reference proteins. The blue squares M and D refer to the HoxC monomer (53.4 kDa, 14.4 mL) and the HoxC dimer (106.8 kDa, 13.16 ml), respectively.

**Table S1.**  $\nu(\text{C}\equiv\text{O})$  and  $\nu(\text{C}\equiv\text{N})$  stretching modes for the active site redox states of HoxC and RH.

| Protein                     | Redox state                      | $\nu(\text{C}\equiv\text{O})$ | $\nu(\text{C}\equiv\text{N})$ | Reference               |
|-----------------------------|----------------------------------|-------------------------------|-------------------------------|-------------------------|
| HoxC <sub>ai</sub>          | Ni <sub>r</sub> -S <sub>I</sub>  | 1952                          | 2066, 2084                    | This work               |
| HoxC <sub>ai</sub>          | Ni <sub>r</sub> -S <sub>II</sub> | 1941                          | 2064, 2077                    | This work               |
| HoxC <sub>ox</sub>          | Ni <sub>r</sub> -B'              | 1969                          | n.d.                          | This work               |
| HoxC <sub>ox</sub>          | Ni <sub>r</sub> -B''             | 1978                          | 2081, 2090                    | This work               |
| HoxC'                       | Ni-L                             | 1889                          | n.d.                          | This work               |
| RH, as-isolated             | Ni <sub>a</sub> -S               | 1943                          | 2071, 2081                    | <sup>5</sup>            |
| RH, H <sub>2</sub> -reduced | Ni <sub>a</sub> -C               | 1961                          | 2072, 2081                    | <sup>5-7</sup>          |
| RH, H <sub>2</sub> -reduced | Ni <sub>a</sub> -SR              | 1948                          | 2058, 2073                    | <sup>6,7</sup>          |
| RH, oxidized                | Ni <sub>r</sub> -B               | 1963/1965*                    | 2089, 2097                    | This work, <sup>6</sup> |

\*The 1965 cm<sup>-1</sup> band identified in reference <sup>6</sup> represents the 1963 cm<sup>-1</sup> band in the present work. In the previous study, the amount of Ni<sub>r</sub>-B was too low to allow an unambiguous assignment. n.d., not detected.

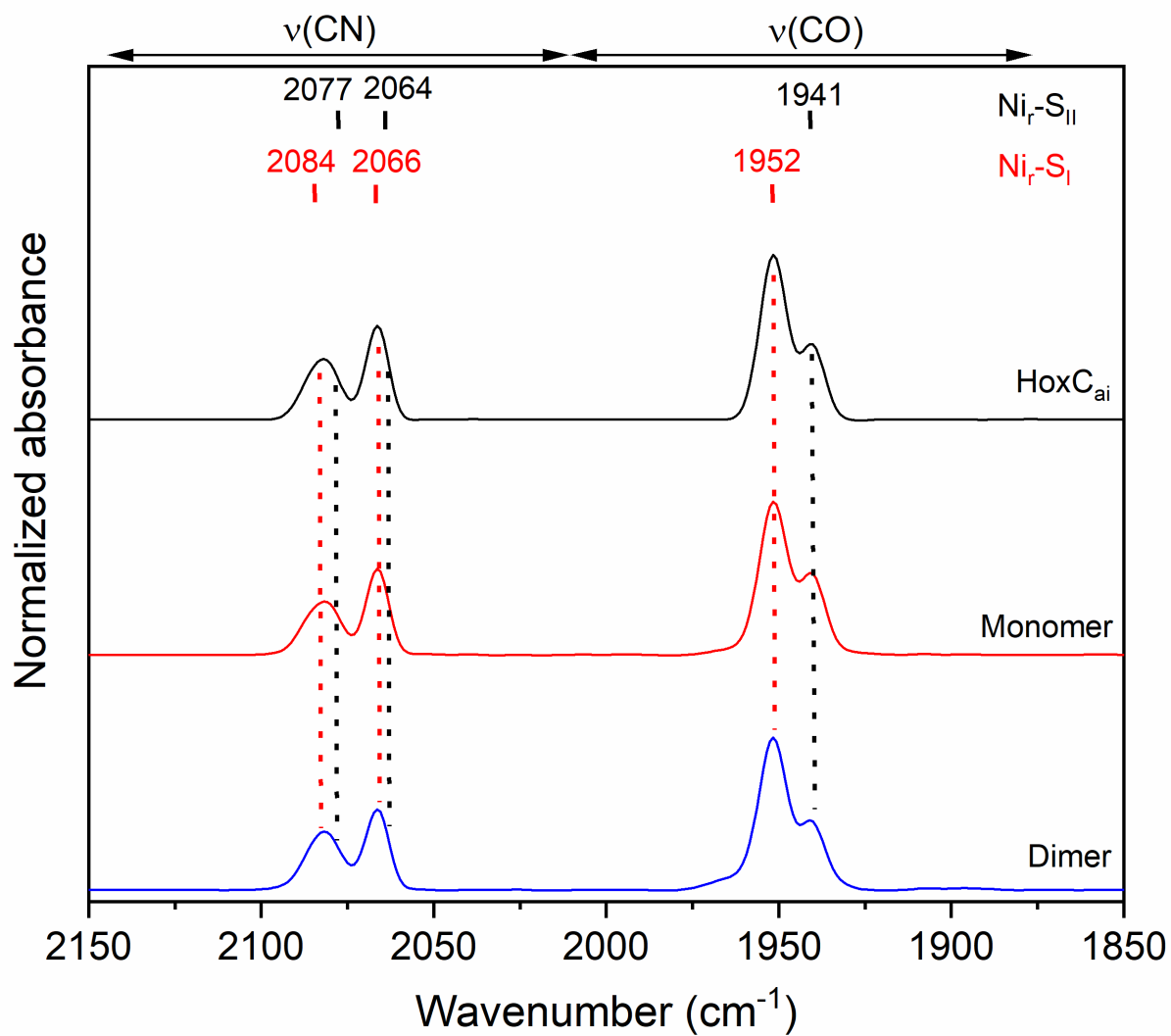


**Figure S4.** IR spectra of HoxC normalized to protein concentration in 50 mM Tris-HCl, 150 mM NaCl at pH 8.0 after Strep-Tactin affinity chromatography (black trace) and after gel filtration isolating monomeric (red trace) and dimeric (blue trace) HoxC.

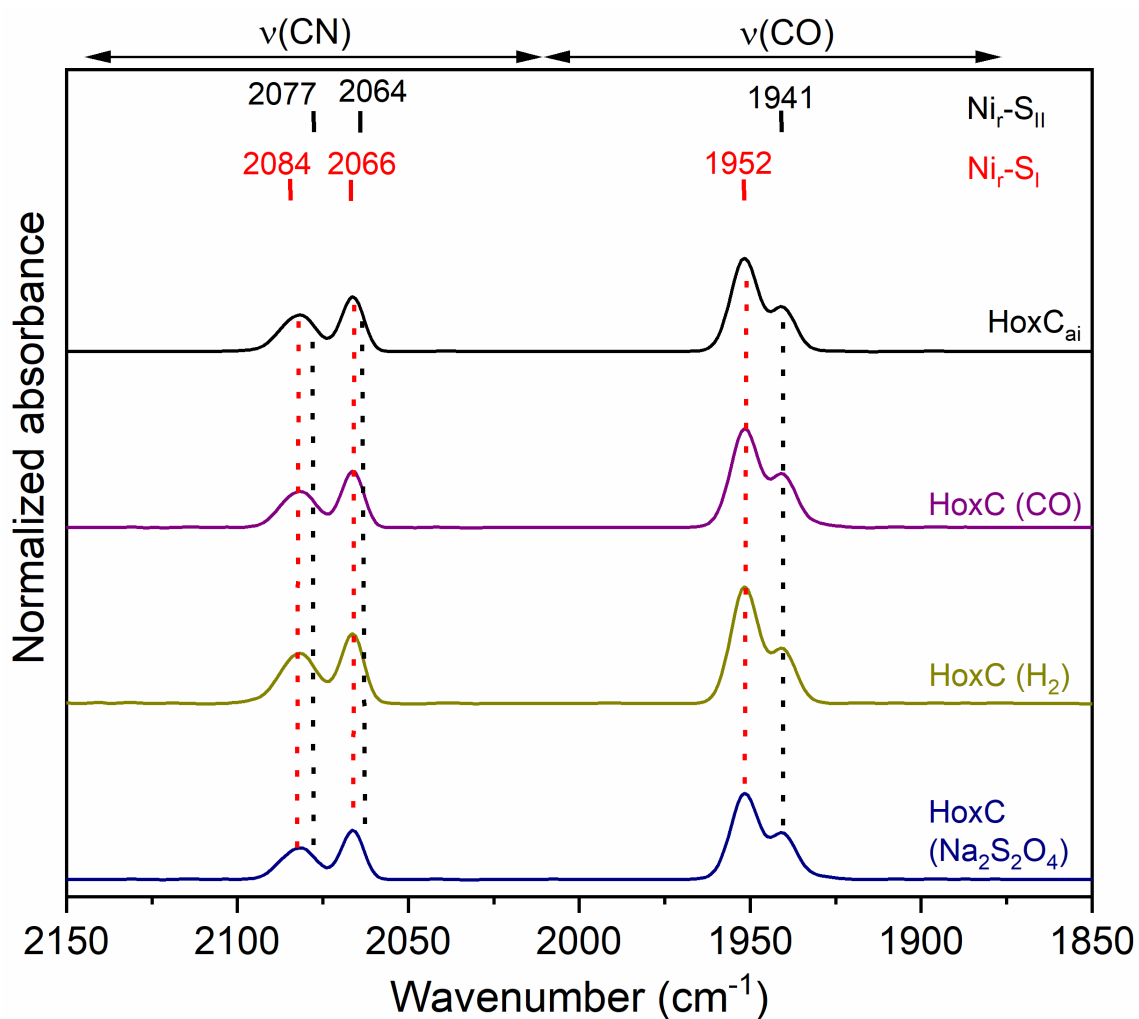


**Figure S5.** IR spectra of HoxC<sub>ai</sub> normalized to protein concentration in 50 mM Tris-HCl, 150 mM NaCl at pH 8.0. From top to bottom: as-isolated (black trace), treated with 1 bar of humidified CO gas for 30 min (purple trace), treated with 1 bar of humidified H<sub>2</sub> gas for 2 h (dark yellow trace) and treated with a 5 molar excess of sodium dithionite (blue trace). Red and black dotted lines denote the respective CO and CN modes of Ni<sub>r</sub>-S<sub>I</sub> and Ni<sub>r</sub>-S<sub>II</sub>.

## TDDFT calculations

To calculate UV-Vis absorptions, we first compiled an active site model carrying low-spin Ni<sup>II</sup> and Fe<sup>II</sup> featuring a hydroxo ligand in bridging position between the metal ions. Geometry optimization was carried out as described in Materials and Methods, resulting in structure **1** (Figure S5). The optimization resulted in a remarkable structural rearrangement, as one of the bridging cysteines lost its connection to Ni. In fact, the corresponding Ni–S interatomic distance was 3.50 Å. Notably, a similar observation has been previously made for an analogous structure, which, however, was a larger QM-cluster model comprising 288-atoms and, thus, considered the geometric constraints imposed by the active-site surroundings on the metals first coordination spheres in a more accurate way.<sup>8</sup> Remarkably, among all active site species that were investigated with this particular model, only the species having a Ni<sup>II</sup>Fe<sup>II</sup> core bridged by either a hydroxo or a water ligand showed such large (non-binding) distance of about 2.9 Å between the bridging cysteine sulfur and the Ni atom.<sup>9</sup> The remaining Ni–S bond distances were in the “normal” range of 2.2–2.3 Å.<sup>8</sup> To evaluate whether the TDDFT results were significantly affected by the large Ni–S distance in our small-size model, we performed an additional, targeted geometry optimization of the Ni<sup>II</sup>Fe<sup>II</sup> low-spin hydroxo-ligated species. In this optimization, the long Ni–S distance of 3.50 Å (structure **1**) was shortened and constrained to ca. 2.9 Å, giving rise to structure **1**<sub>NiS2.9</sub> (not shown). Both **1** and **1**<sub>NiS2.9</sub> were then considered for subsequent TDDFT calculations.

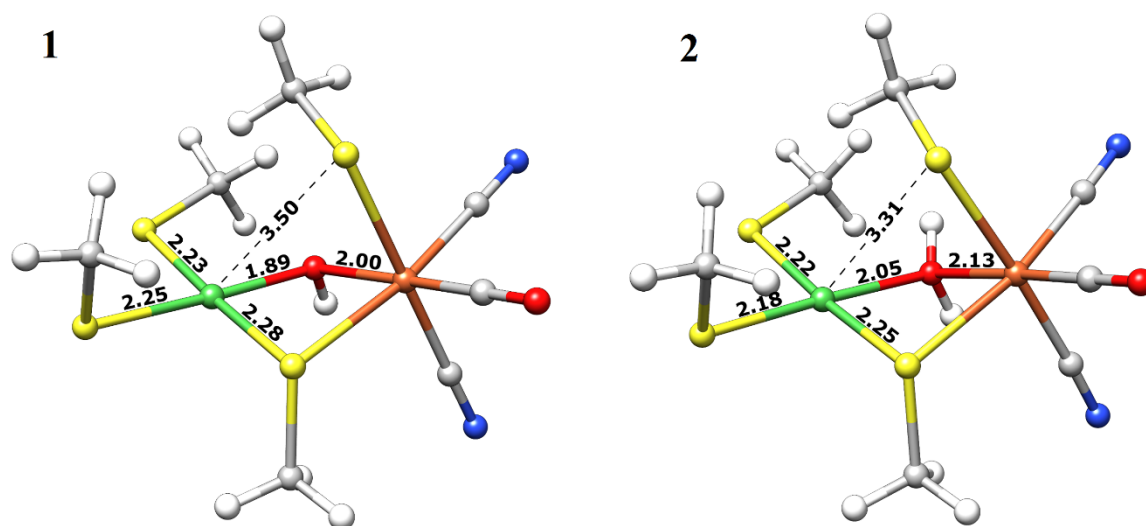


**Figure S6.** Optimized geometry of the low-spin Ni<sup>II</sup>-OH-Fe<sup>II</sup> (**1**) and Ni<sup>II</sup>-HOH-Fe<sup>II</sup> (**2**) models of [NiFe]-hydrogenase active site. Selected interatomic distances are given in Å. Atoms are colored according to the following scheme: Ni, green; Fe, orange; N, blue; O, red; S, yellow; C, grey; H, white.

**Table S2.** TDDFT excitation energies and corresponding oscillator strengths computed for structures **1** and **1<sub>NiS2.9</sub>**.

| Exc. state number | Wavelength of the computed absorption (nm) |                           | Oscillator strength |                           |
|-------------------|--|---------------------------|---------------------|---------------------------|
|                   | <b>1</b>                                   | <b>1<sub>NiS2.9</sub></b> | <b>1</b>            | <b>1<sub>NiS2.9</sub></b> |
| 1                 | 703.54                                     | 897.73                    | 0.0004              | 0.0006                    |
| 2                 | 668.16                                     | 697.04                    | 0.0001              | 0.0005                    |
| 3                 | 653.72                                     | 675.00                    | 0.0002              | 0.0002                    |
| 4                 | 589.75                                     | 624.96                    | 0.0001              | 0.0002                    |
| 5                 | 523.13                                     | 504.38                    | 0.0009              | 0.0003                    |
| 6                 | 443.17                                     | 435.44                    | 0.0034              | 0.0042                    |
| 7                 | 420.70                                     | 421.73                    | 0.0047              | 0.0037                    |
| 8                 | 394.29                                     | 378.37                    | 0.0012              | 0.0007                    |
| 9                 | 355.17                                     | 355.94                    | 0.0019              | 0.0026                    |
| 10                | 349.95                                     | 353.08                    | 0.0024              | 0.0006                    |
| 11                | 337.67                                     | 340.19                    | 0.0400              | 0.0407                    |
| 12                | 308.06                                     | 307.42                    | 0.0065              | 0.0091                    |
| 13                | 286.96                                     | 291.07                    | 0.0336              | 0.0052                    |
| 14                | 284.65                                     | 286.78                    | 0.0914              | 0.0025                    |
| 15                | 284.17                                     | 280.02                    | 0.0224              | 0.0033                    |
| 16                | 271.90                                     | 278.09                    | 0.0600              | 0.1266                    |
| 17                | 269.32                                     | 272.49                    | 0.0010              | 0.0339                    |
| 18                | 268.91                                     | 272.03                    | 0.0045              | 0.0577                    |
| 19                | 259.06                                     | 265.21                    | 0.0022              | 0.0081                    |
| 20                | 257.34                                     | 260.13                    | 0.0138              | 0.0005                    |

Notably, the overall wavelength and oscillator strength patterns for structures **1** and **1<sub>NiS2.9</sub>** were essentially the same (Table S2), indicating that the calculated UV-vis absorptions are not significantly affected by the large Ni–S interatomic distance of 3.5 Å. Hence, only the results of the structure **1**-derived calculations are graphically represented as blue sticks in Figure S6.

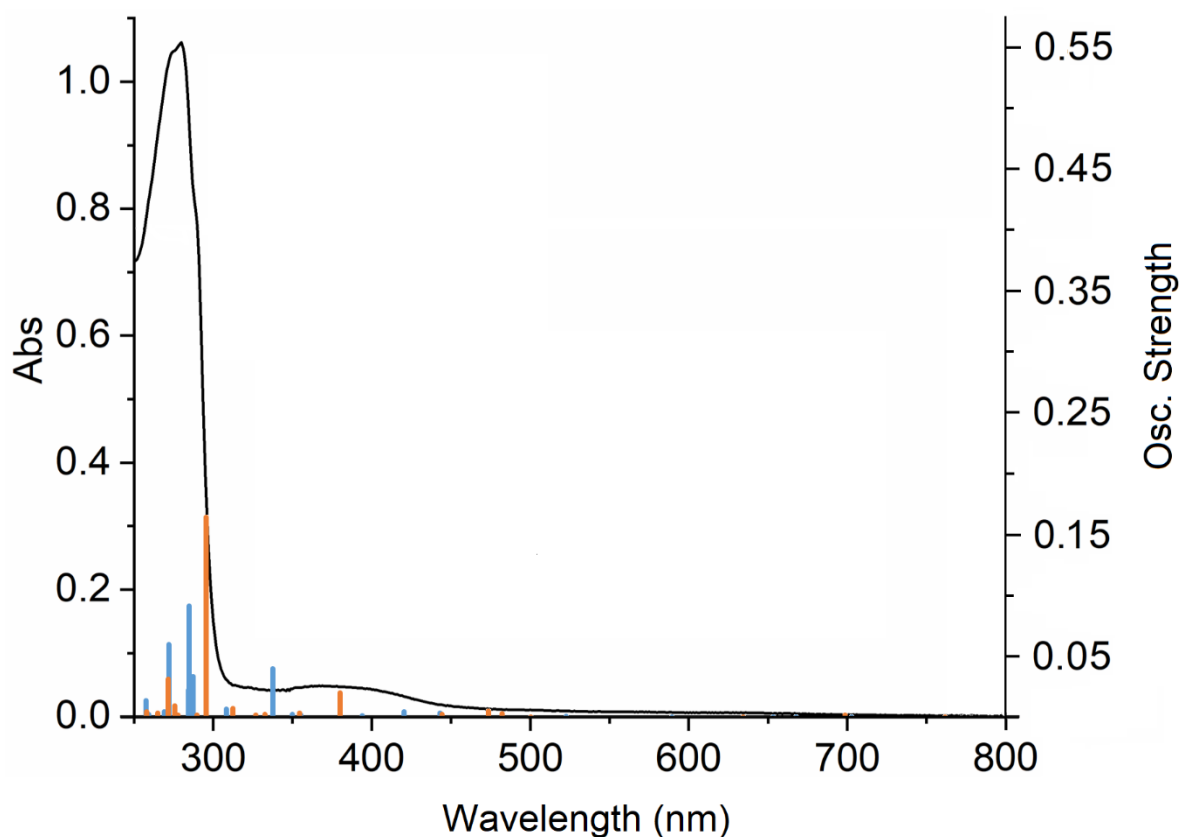


**Figure S7.** Superimposition of TDDFT-computed UV-Vis absorptions for the Ni<sup>II</sup>-OH-Fe<sup>II</sup> and Ni<sup>II</sup>-HOH-Fe<sup>II</sup> species (blue and orange sticks, respectively, the length of which is proportional to their oscillator strengths) on the experimental UV-Vis spectrum of [NiFe]-HoxC (black solid line).

TDDFT-derived energies errors lie typically in the range of 0.2–0.4 eV.<sup>10</sup> Thus, the absorption computed at 338 nm for structure **1** (Table S2, Figure S6) should correspond to the experimentally determined maximum of absorption at 370 nm (Figure 2A). The relatively strong TDDFT absorptions below 300 nm are also consistent with the experimental spectrum. The absorption band at 390 nm in the experimental spectrum (Figure 2A) was, however, not represented by any TDDFT-derived wavelength (Table S2). In fact, no absorptions with appreciable oscillator strengths were computed to reside at wavelengths larger than 338 nm. This prompted us to investigate further the experimentally determined band at 390 nm. We considered the possibility that the hydroxo ligand in **1** undergoes protonation. The corresponding geometry optimization resulted in structure **2** (Figure S5). Consistent with the observations for a large-size Ni<sup>II</sup>Fe<sup>II</sup> low-spin model featuring bridging water,<sup>8</sup> structure **2** also contained an enlarged Ni–S distance of 3.3 Å.

The TDDFT-derived calculations of the UV-vis absorptions for structure **2** are summarized in Table S3 and the absorptions graphically represented as orange sticks in Figure S6. In contrast to the results for structure **1**, structure **2** revealed an absorption at 380 nm, which probably corresponds to the experimentally determined band at 390 nm. Strong absorptions were also calculated for wavelengths below 300 nm, (e.g. at 296 nm, Table S3), which is consistent with the calculations for structure **1** (Table S2).

**Table S3.** TDDFT excitation energies and corresponding oscillator strengths computed for structure **2**.

| Exc. state number | Wavelength of the computed absorption (nm) | Oscillator strength |
|-------------------|--|---------------------|
| 1                 | 823.27                                     | 0.0019              |
| 2                 | 762.58                                     | 0.0002              |
| 3                 | 699.31                                     | 0.0018              |
| 4                 | 635.03                                     | 0.0002              |
| 5                 | 500.58                                     | 0.0004              |
| 6                 | 482.66                                     | 0.0030              |
| 7                 | 473.92                                     | 0.0050              |
| 8                 | 444.41                                     | 0.0022              |
| 9                 | 379.87                                     | 0.0202              |
| 10                | 354.61                                     | 0.0037              |
| 11                | 332.62                                     | 0.0026              |
| 12                | 326.91                                     | 0.0019              |
| 13                | 312.48                                     | 0.0074              |
| 14                | 295.52                                     | 0.1642              |
| 15                | 289.47                                     | 0.0021              |
| 16                | 277.69                                     | 0.0016              |
| 17                | 275.52                                     | 0.0096              |
| 18                | 271.27                                     | 0.0313              |
| 19                | 264.89                                     | 0.0036              |
| 20                | 257.99                                     | 0.0048              |

Next, we analyzed in detail the electronic contributions giving rise to the theoretical absorptions at 338 nm for structure **1** and at 380 nm for structure **2**. The molecular orbitals (MOs) mainly involved in determining these absorptions and their relative coefficients in the respective CI expansions are reported in Table S4. Note that MO 104 is the lowest unoccupied molecular orbital for both species. Graphic representations of the MOs are provided in Figure S7 (structure **1**) and Figure S8 (structure **2**). In both the Ni<sup>II</sup>-HOH-Fe<sup>II</sup> and the Ni<sup>II</sup>-OH-Fe<sup>II</sup> species, the analyzed absorptions in the near UV appear to be due to an electronic redistribution mainly centered at the Ni ion and its first coordination sphere.

**Table S4.** MOs involved in the TDDFT transitions at 338 nm and 380 nm computed for the Ni<sup>II</sup>-OH-Fe<sup>II</sup> species (structure 1) and Ni<sup>II</sup>-HOH-Fe<sup>II</sup> species (structure 2), respectively.

| Ni <sup>II</sup> -OH-Fe <sup>II</sup> (structure 1) |          |         | Ni <sup>II</sup> -HOH-Fe <sup>II</sup> (structure 2) |          |         |
|---|----------|---------|--|----------|---------|
| Starting MO   | Final MO | Coeff.* | Starting MO  | Final MO | Coeff.* |
| 102   | 104      | 0.55    | 102  | 104      | 0.48    |
| 92  | 104      | 0.19    | 92   | 104      | 0.22    |
| 95  | 104      | 0.17    | 99   | 104      | 0.19    |

\* Module of the coefficients in the CI expansion

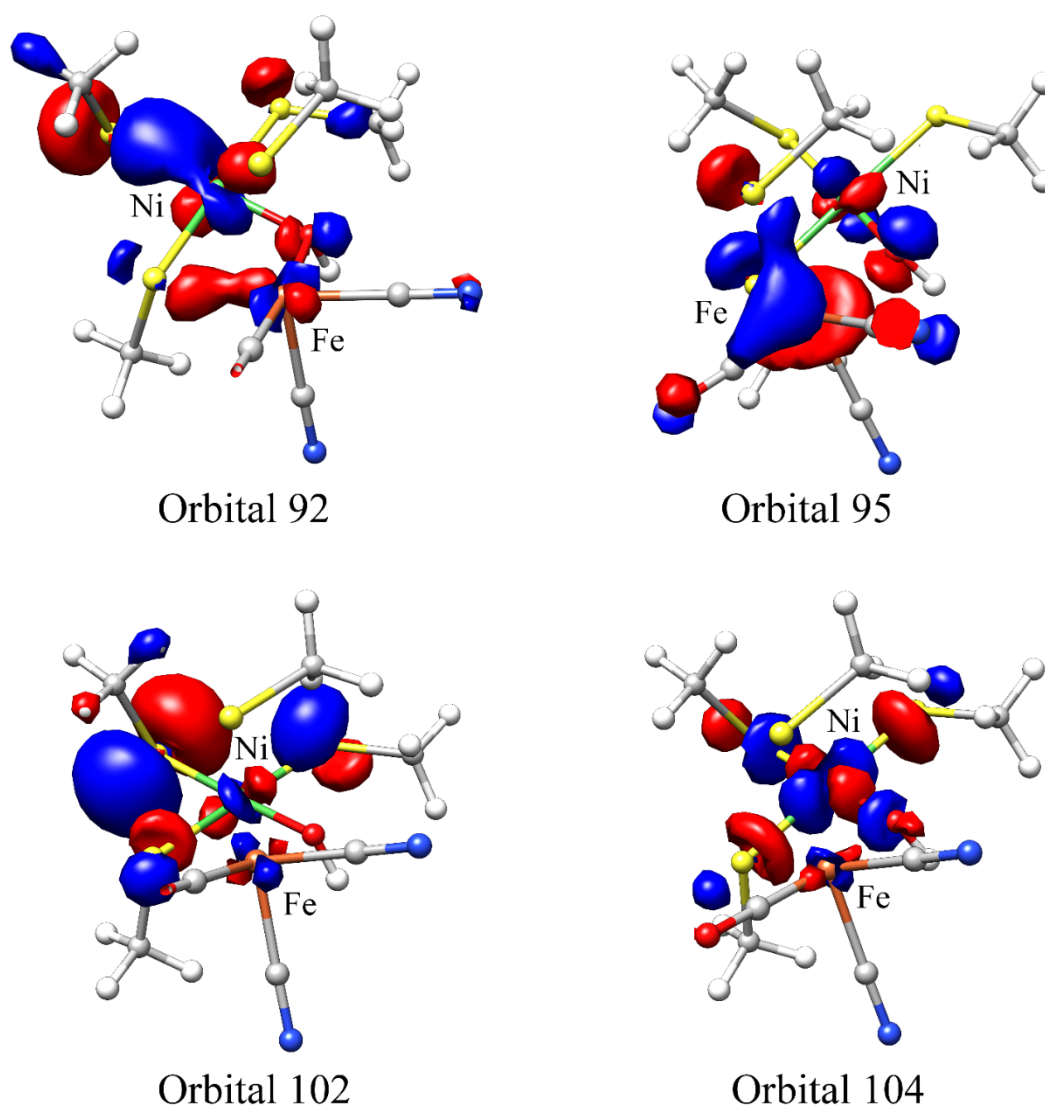


**Figure S8.** Occupied MOs (92, 95, 102) and the virtual MO (104, LUMO) involved in the TDDFT transition at 338 nm computed for the Ni<sup>II</sup>-OH-Fe<sup>II</sup> species (structure 1). Color code is as in Fig. S5. Some bonds were omitted from the graphical representation to better show the MOs characters

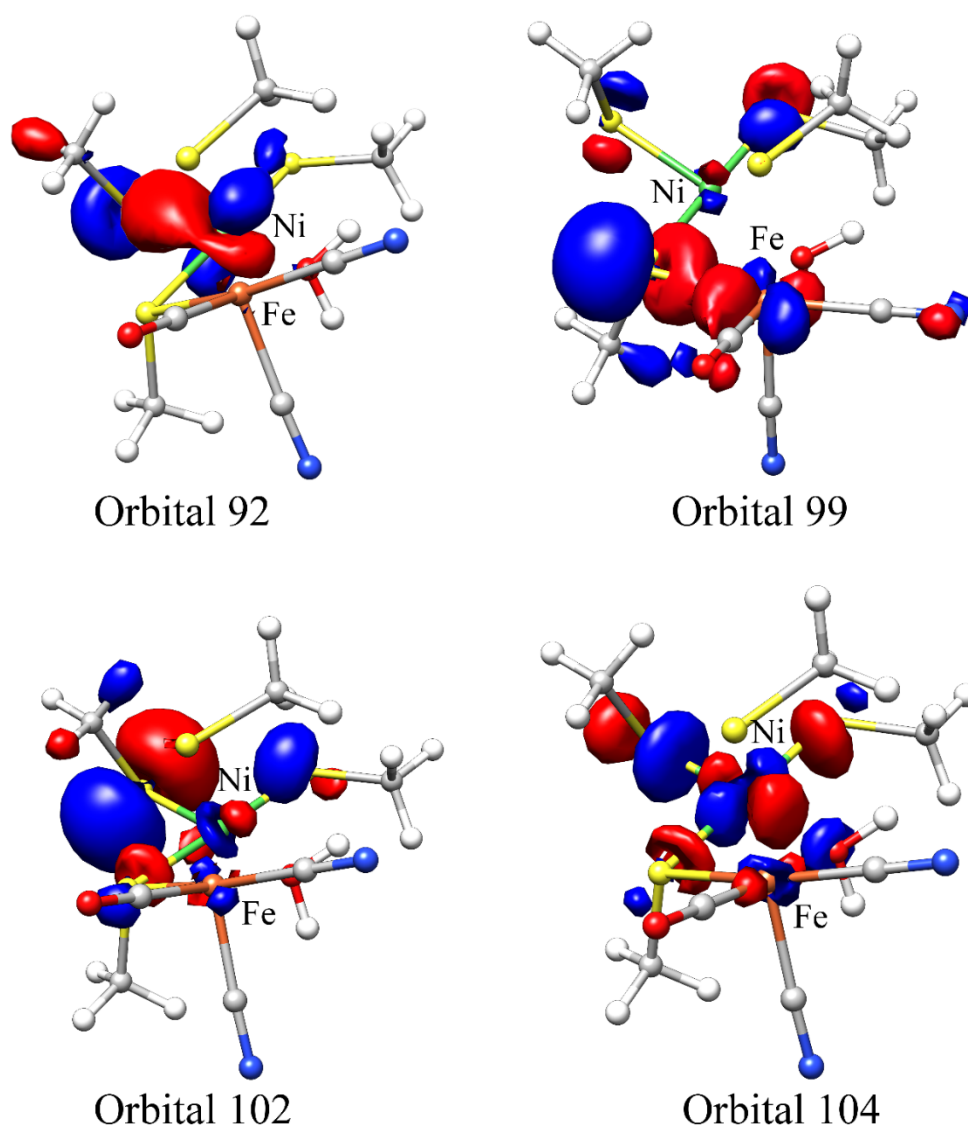


**Figure S9.** Occupied MOs (92, 99, 102) and the virtual MO (104, LUMO) involved in the TDDFT transition at 380 nm computed for the Ni<sup>II</sup>-HOH-Fe<sup>II</sup> species (structure **2**). Color code is as in **Fig. S5**. Some bonds were omitted from the graphical representation, to better show the MOs characters

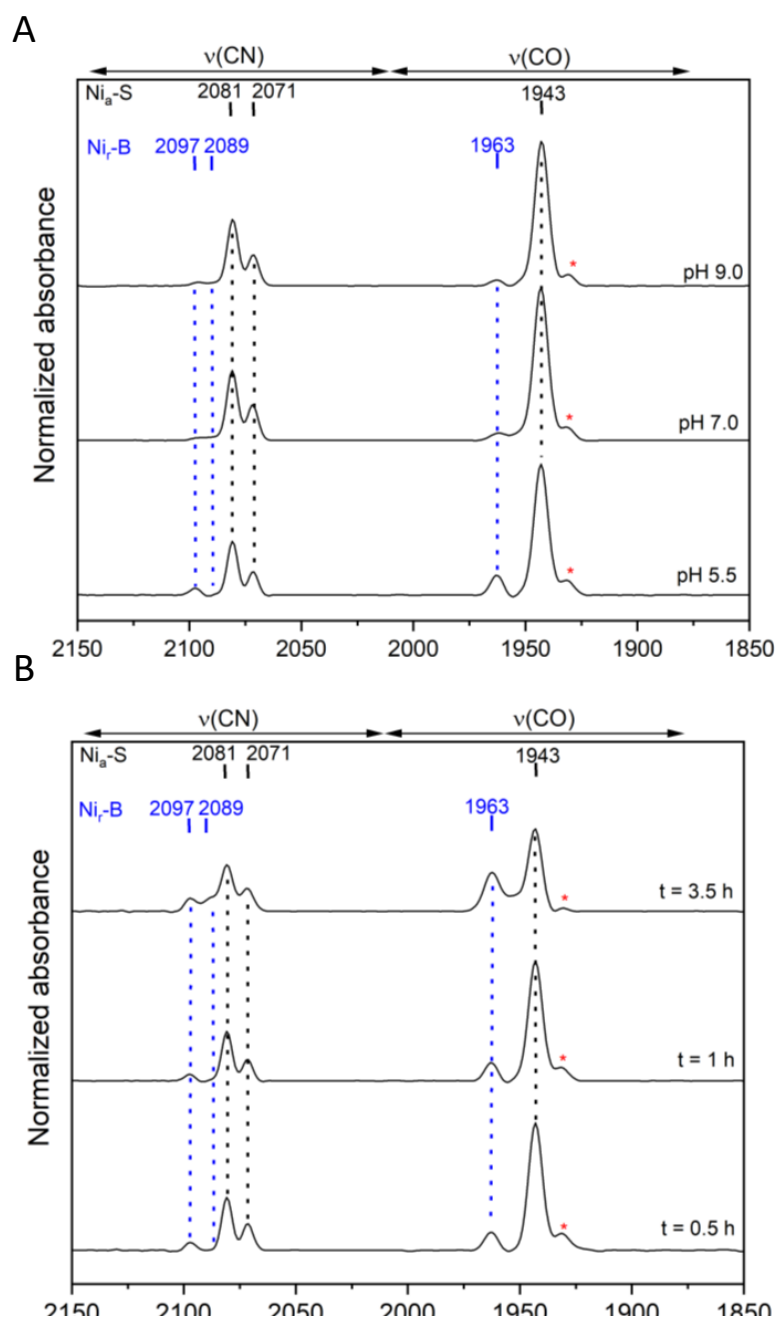


**Figure S10.** IR spectroscopic investigation of as-isolated RH. **(A)** IR spectra of RH normalized to protein concentration at different pH values. At pH 5.5 an increase of species attributable to Ni<sub>r</sub>-B could be detected, based on the  $\nu(\text{C}\equiv\text{O})$  stretching mode found at 1963  $\text{cm}^{-1}$ . Modes related to Ni<sub>a</sub>-S and Ni<sub>r</sub>-B are depicted in black and blue, respectively. The CO absorption of an unknown species is marked with a red asterisk.<sup>6</sup> **(B)** Time-dependent IR spectra of RH at pH 5.5 at  $t = 0.5$  h,  $t = 1$  h,  $t = 3.5$  h display an increase of the Ni<sub>r</sub>-B species. Notably,  $\nu(\text{C}\equiv\text{N})$  stretching modes of the Ni<sub>r</sub>-B redox state (confirmed by EPR data, **Fig. S9**) at these band positions were not detected in a previous study.<sup>6</sup>

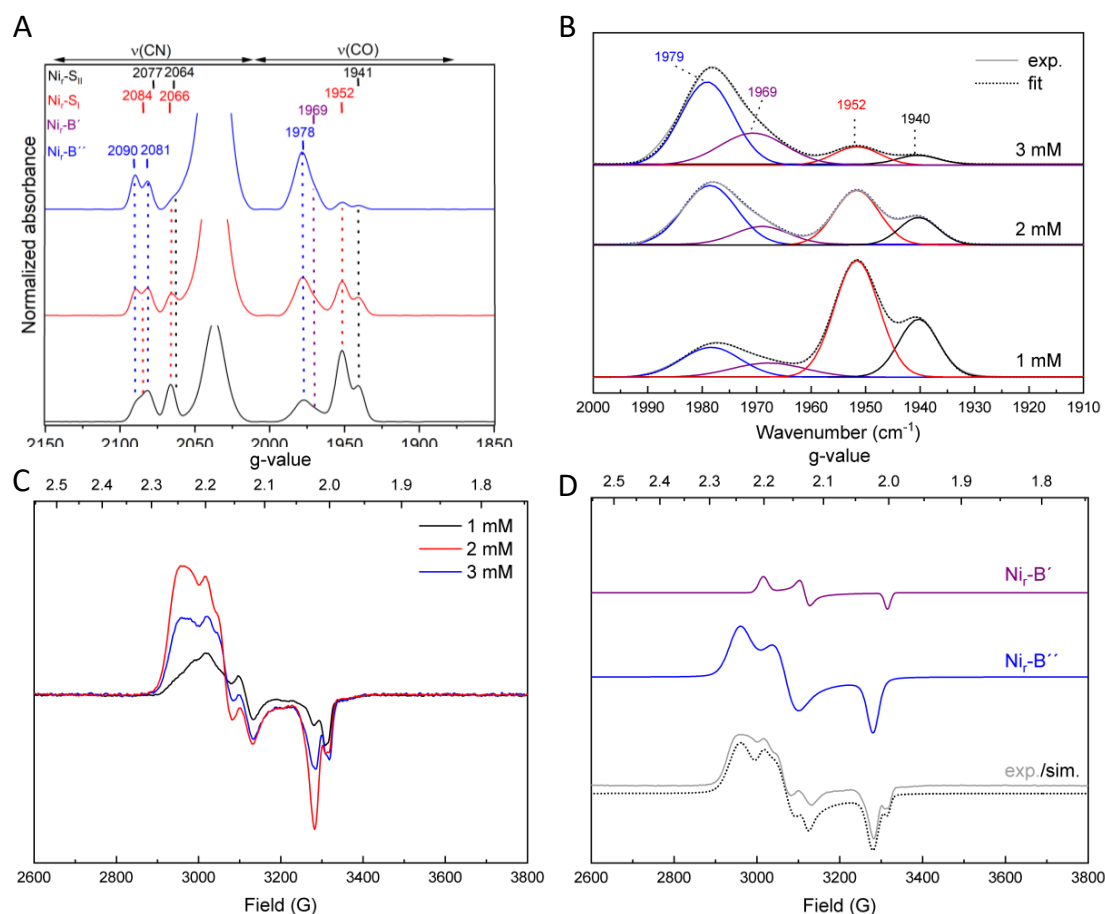


**Figure S11.** (A) IR spectra normalized to protein concentration of HoxC treated with 1 equivalent (eq.), black trace, 2 eq., red trace, and 3 eq., blue trace, of  $K_3Fe(CN)_6$ . Dotted lines indicate the CO and CN modes of the active site in the as isolated ( $Ni_{I-S_I}$  and  $Ni_{I-S_{II}}$ , red and black) and oxidized state (blue), respectively.  $HoxC_{ox}$  is represented by the 1969 and 1978 cm<sup>-1</sup> CO modes, that increase with  $K_3Fe(CN)_6$  concentration. (B) Band fitting of the CO modes exhibits the conversion from  $Ni_{I-S}$  (1952 cm<sup>-1</sup>) and  $Ni_{I-S_{II}}$  (1941 cm<sup>-1</sup>) states to the  $Ni_{I-B'}$  (1969 cm<sup>-1</sup>) and  $Ni_{I-B''}$  (1978 cm<sup>-1</sup>) species, depending on the amount of added  $K_3Fe(CN)_6$ . (C) EPR spectra of 1.0 mM HoxC treated with 1 eq., 2 eq. and 3 eq. of  $K_3Fe(CN)_6$  (color code as in S7A). (D) Simulation of two  $Ni_{I-B'}$  and  $Ni_{I-B''}$  rhombic signals for the EPR spectrum of  $HoxC_{ox}$ . Spectral contribution of paramagnetic  $K_3Fe(CN)_6$  was avoided by working with a small excess (2-3 eq.) of the chemical, which was converted completely to the diamagnetic  $K_4Fe(CN)_6$ . IR spectra were recorded to confirm the absence of  $K_3Fe(CN)_6$  in the EPR samples (Fig. S7A). Prolonged incubation with  $K_3Fe(CN)_6$  induces cofactor degradation as evident from the decrease of the EPR signal of the  $Ni^{III}$  species with 3 mM of  $K_3Fe(CN)_6$  (Fig. S7C). Prolonged incubation with  $K_3Fe(CN)_6$  led also to the disappearance of CO and CN features of the active site (data not shown).

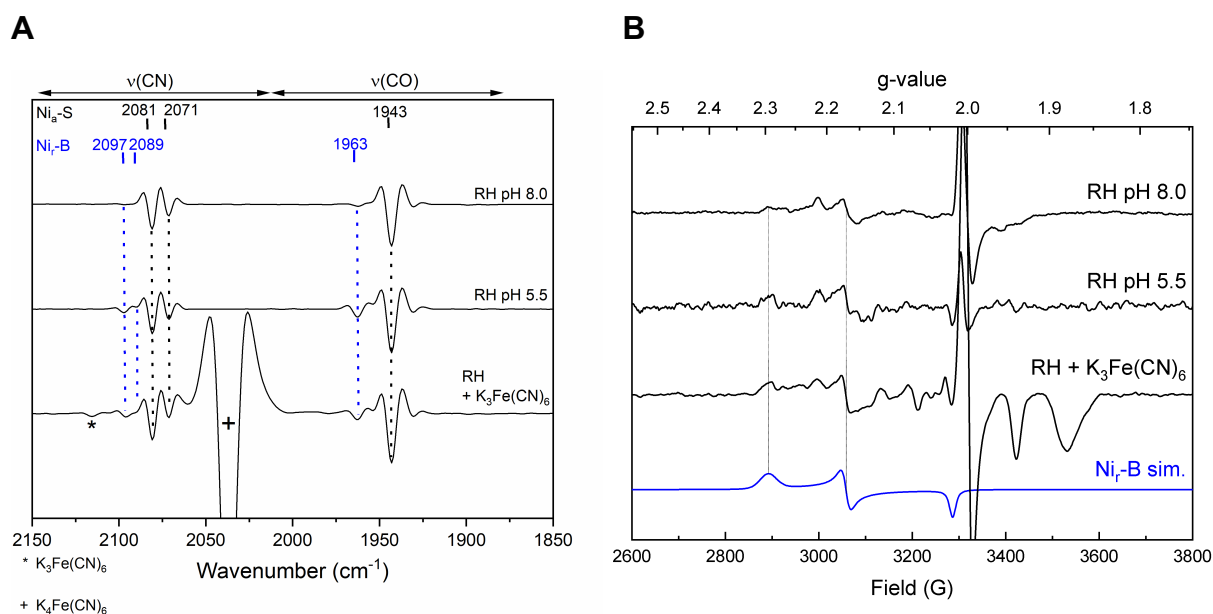


**Figure S12.** (A) Second derivatives of IR spectra recorded from the RH at pH values of 8.0, pH 5.5 and at pH 8.0 with an excess of K<sub>3</sub>Fe(CN)<sub>6</sub>. Air or chemical oxidation increased the spectral contribution of Ni<sub>r</sub>-B species. Modes related to the Ni<sub>a</sub>-S and Ni<sub>r</sub>-B modes are labelled in black and blue, respectively. The asterisk symbol corresponds to the ν(C≡N) stretching vibration of K<sub>3</sub>Fe(CN)<sub>6</sub> and the plus symbol to the ν(C≡N) mode of K<sub>4</sub>Fe(CN)<sub>6</sub> as shown in **Fig. S1**. The presence of K<sub>4</sub>Fe(CN)<sub>6</sub> confirms that electrons can be extracted from RH, accompanied by an increase of the Ni<sub>r</sub>-B species. (B) EPR spectra of RH recorded at 80 K and pH 8.0, pH 5.5 and pH 8.0 with an excess of K<sub>3</sub>Fe(CN)<sub>6</sub> revealed a mixture of different Ni(III) species discernible by the nickel related signal in the region g = 2.3 - 2.0. Especially at pH 5.5 or after oxidative treatment with an excess of K<sub>3</sub>Fe(CN)<sub>6</sub> signals assigned to a standard Ni<sub>r</sub>-B state (g<sub>1</sub> = 2.296; g<sub>2</sub> = 2.170 g<sub>3</sub> = 2.020, blue trace simulation) increased. Furthermore, signals below g = 2.0 indicate the presence of additional paramagnetic species. These are possibly related to damaged [4Fe4S] cluster forming [3Fe4S] cluster or further degradation products. Spectra are normalized to the protein concentration of RH (0.3 mM at pH 8.0, 0.1 mM at pH 5.5, and 0.2 mM with excess of K<sub>3</sub>Fe(CN)<sub>6</sub> at pH 8).

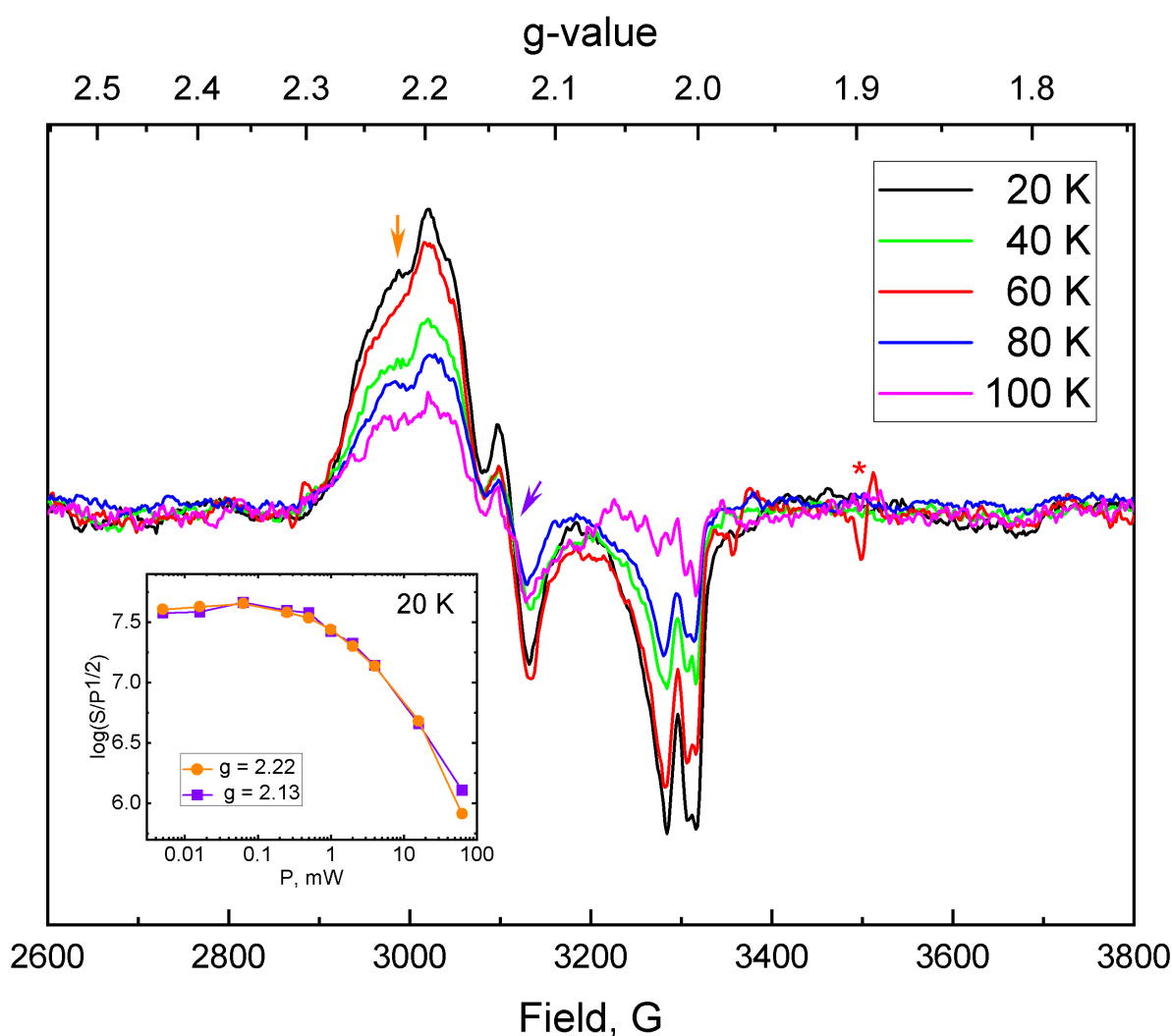


**Figure S13.** Temperature dependent EPR spectra of HoxC oxidized with 6 eq. of  $K_3Fe(CN)_6$  in 50 mM Tris-HCl, 150 mM NaCl at pH 8.0. The inset shows the microwave power dependent saturation of signals attributed to  $Ni_{I-B''}$  at  $g = 2.22$  and  $Ni_{I-B'}$  at  $g = 2.13$ . The field position is indicated by an orange and purple arrow, respectively. Overall the temperature and power dependent behavior exhibits large similarities in the two different signals. Notably, FeS cluster-derived signals were absent in the HoxC preparation, in which the small HoxB subunit was missing. The signal labelled with an asterisk originates from microwave reflections caused by the instability of the EPR resonator at this temperature.

**Table S5.** EPR-derived g-values extracted from spectra obtained for HoxC in different redox states of the active site.

| Redox state          | EPR g-values |       |       |
|----------------------|--------------|-------|-------|
|                      | g1           | g2    | g3    |
| Ni <sub>r</sub> -B'  | 2.203        | 2.132 | 2.004 |
| Ni <sub>r</sub> -B'' | 2.246        | 2.164 | 2.025 |
| Ni-L                 | 2.305        | 2.095 | 2.053 |

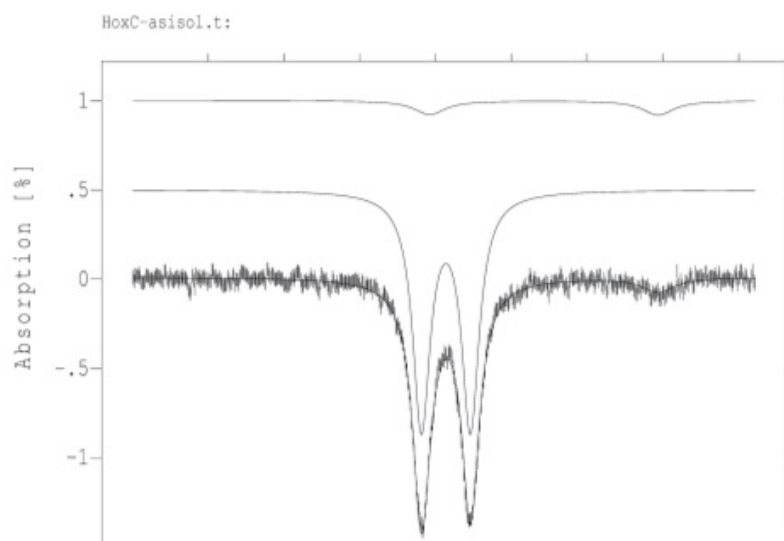
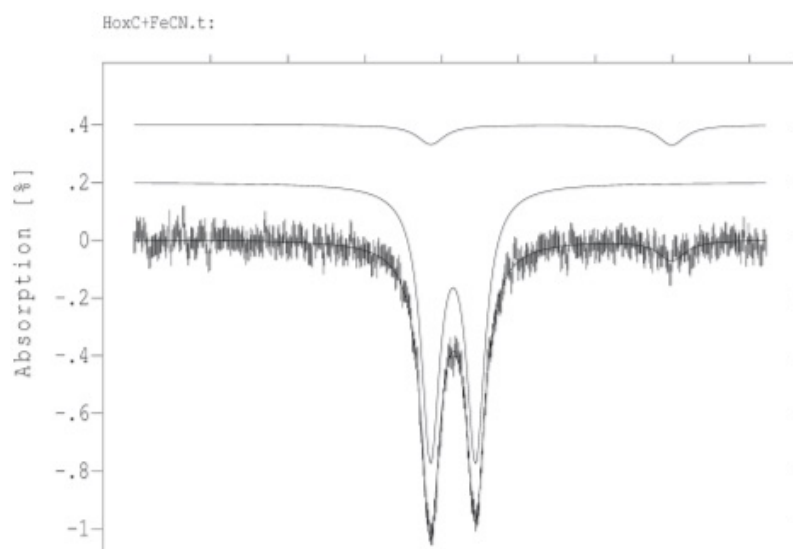
**Table S6.** Parameters obtained from the simulations of the Mössbauer spectra of HoxC and RH from *R. eutropha*.

| Protein | Redox state   | Isomer shift ( $\delta$ mm s <sup>-1</sup> ) | Quadrupole splitting ( $\Delta E_Q$ mm s <sup>-1</sup> ) | Relative area (% total iron) |
|---------|---|--|--|------------------------------|
| HoxC    | Ni <sub>r</sub> -S <sub>I</sub> /Ni <sub>r</sub> -S <sub>II</sub> | 0.14   | 0.65   | 92                           |
| HoxC    | Ni <sub>r</sub> -B'/''  | 0.15   | 0.59   | 90                           |
| *RH     | Ni <sub>a</sub> -S  | 0.1  | 1.6  | 7 <sup>7</sup>               |
| *RH     | Ni <sub>a</sub> -C  | 0.07   | 0.69   | 7 <sup>7</sup>               |

\*Only the isomer shift and the quadrupole splitting of the low-spin Fe<sup>II</sup> of the active site are listed. Values are adapted from ref<sup>7</sup>.

**Table S7.** Comparison of HD and D<sub>2</sub> production rates of different [NiFe]-hydrogenases and isolated large subunits.

| Species     | HD ( $\cdot 10^{-3}$ s <sup>-1</sup> ) | D <sub>2</sub> ( $\cdot 10^{-3}$ s <sup>-1</sup> ) | HD/D <sub>2</sub> | References    |
|-------------|--|--|-------------------|---------------|
| RH (HoxBC)  | 460                                    | 1802   | 0.25              | This work     |
| HoxC        | 0.89                                   | 0.193  | 4.5               | This work     |
| preHoxG     | 0.74                                   | 2.04   | 0.37              | <sup>11</sup> |
| MBH (HoxKG) | 11.21                                  | 12.55  | 0.89              | <sup>11</sup> |

**A****B**

**Figure S14.** Mössbauer spectra of  $^{57}\text{Fe}$ -labelled HoxC in comparison to simulated spectra. (A) as-isolated (B) and chemically oxidized HoxC. Spectra were simulated assuming a major  $\text{Fe}^{\text{II}}$  low-spin species of the catalytic [NiFe]-cofactor ( $\delta = 0.14$ ,  $\Delta E_{\text{Q}} = 0.65 \text{ mm s}^{-1}$  for  $\text{HoxC}_{\text{ai}}$  and  $\delta = 0.15$ ,  $\Delta E_{\text{Q}} = 0.59 \text{ mm s}^{-1}$  for  $\text{HoxC}_{\text{ox}}$ ; see Table S6) in addition to traces of high-spin  $\text{Fe}^{\text{II}}$  ( $\delta = 1.43$ ,  $\Delta E_{\text{Q}} = 3.02 \text{ mm s}^{-1}$  for  $\text{HoxC}_{\text{ai}}$  and  $\delta = 1.43$ ,  $\Delta E_{\text{Q}} = 3.13 \text{ mm s}^{-1}$  for  $\text{HoxC}_{\text{ox}}$ ) representing 8-10 % of the total iron content. The full width at half maximum values are  $0.28 \text{ mm/s}$  for  $\text{HoxC}_{\text{ai}}$  and  $0.29 \text{ mm/s}$  for  $\text{HoxC}_{\text{ox}}$ .

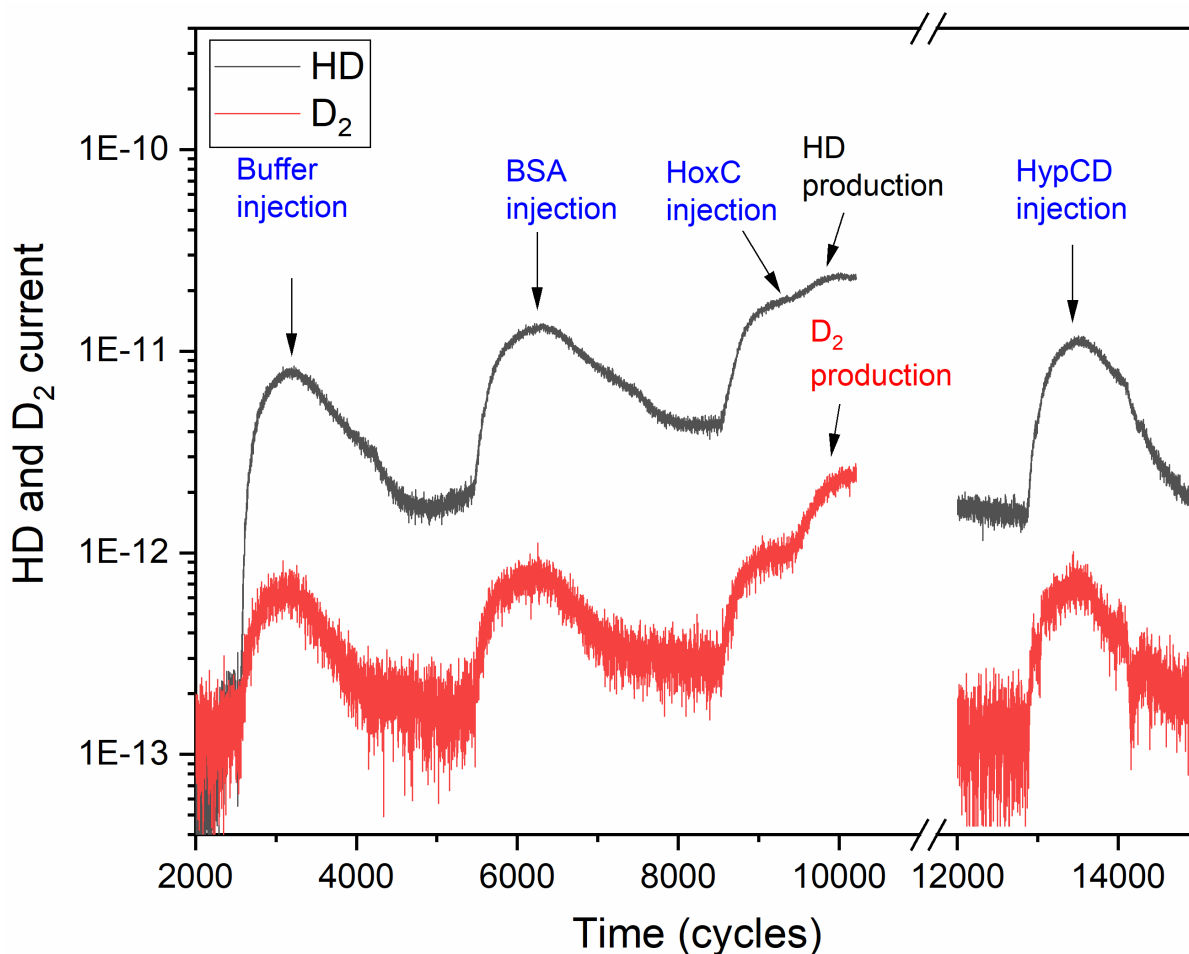


**Figure S15.** Raw data of the current response of the mass spectrometer resulting from changes in the HD and D<sub>2</sub> concentrations as a function of the time. After stabilization of the HD and D<sub>2</sub> gas-derived currents under H<sub>2</sub>-saturating conditions, 10  $\mu$ l of buffer (50 mM K<sub>2</sub>HPO<sub>4</sub>/100 mM citric acid, pH 4.5), 10  $\mu$ l of bovine serum albumin solution (10 mg/ml), 10  $\mu$ l of HoxC solution (10 mg/ml) and 10  $\mu$ l of HypCD<sup>12</sup> solution (10 mg/ml) were injected into the reaction chamber. The mass spectrometer response to changing amounts of HD and D<sub>2</sub> gas was monitored. The electrical signal generated by the spectrometer is directly proportional to the gas concentration in the chamber.<sup>13</sup> Here, the data were not corrected for the continuous decrease in gas concentration, which was caused by the vacuum pipeline connecting the measurement chamber with the detector of the mass spectrometer. Notably, the gas loss was considered for calculating all the catalytic HD and D<sub>2</sub> production rates in this manuscript. 1 cycle took 0.8 s.

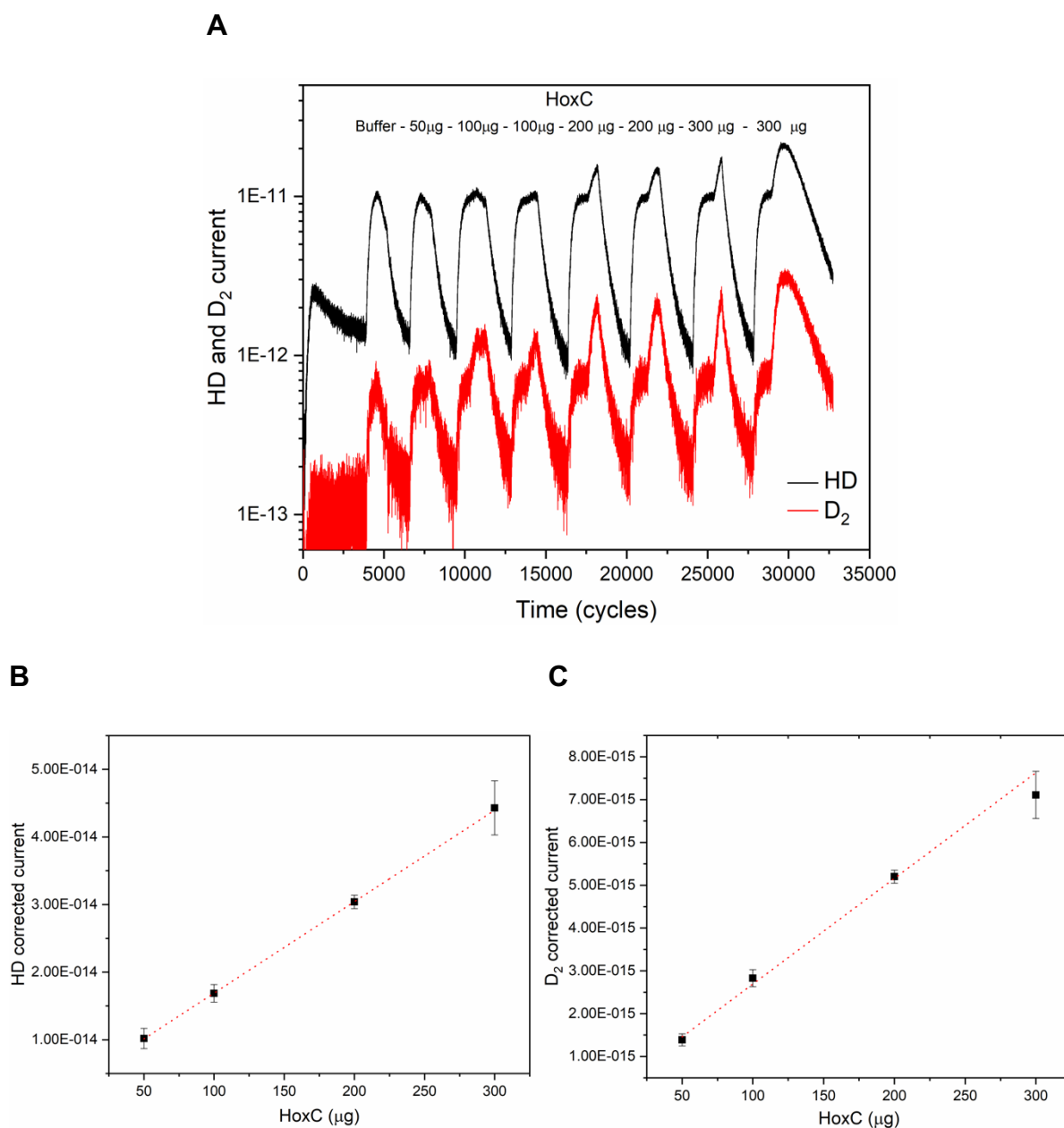


**Figure S16.** HD and D<sub>2</sub> production as a function of HoxC concentration. **(A)** Raw-data of HD- and D<sub>2</sub>-mediated electric response as a function of the time. After stabilization of the HD and D<sub>2</sub> currents under H<sub>2</sub>-saturating conditions, different HoxC quantities (50 – 300 μg) were injected into the reaction chamber, and the mass spectrometer response to changes in the HD and D<sub>2</sub> gas concentration was monitored. 1 cycle took 0.8 s. Changes in the HD and D<sub>2</sub> concentration upon buffer addition were subtracted from the HD and D<sub>2</sub> concentration changes upon addition of HoxC protein. **(B)** HD corrected-current response as a function of HoxC concentration. **(C)** D<sub>2</sub> corrected-current response as a function of HoxC concentration. Both the HD and D<sub>2</sub> production rates correlated linearly with the HoxC concentration. Measurements were performed at pH 4.5 (50 mM K<sub>2</sub>HPO<sub>4</sub>/100 mM citric acid pH 4.5).

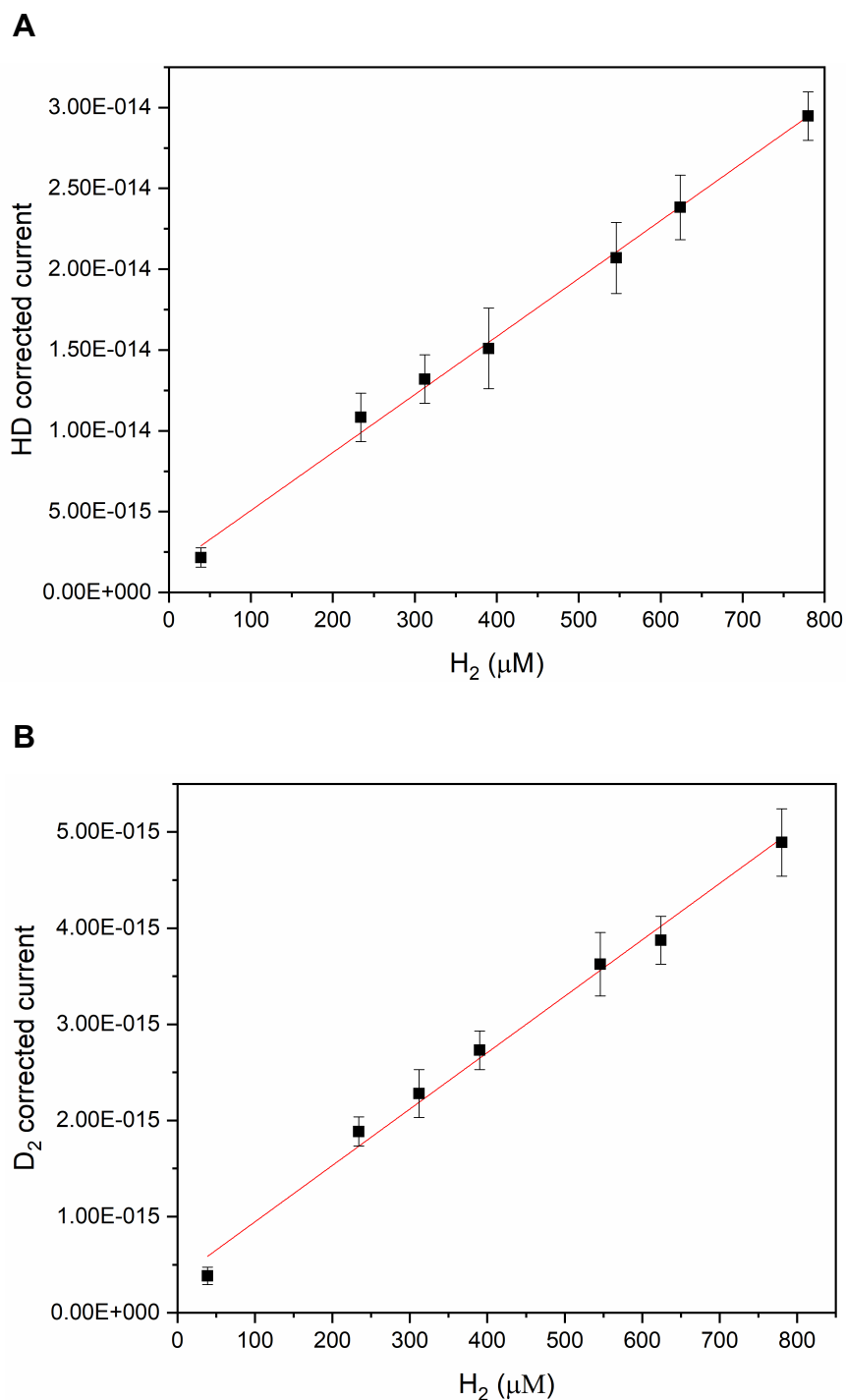


**Figure S17.** Corrected HD (**A**) and D<sub>2</sub> (**B**) current responses as a function of H<sub>2</sub> concentration. Different ratios of H<sub>2</sub> and N<sub>2</sub> saturated buffers were mixed, and the corresponding H<sub>2</sub> concentration was calculated considering 780 μM (1.57 mg/L) the maximum H<sub>2</sub> solubility in water at 20 °C (<http://www.molecularhydrogeninstitute.com/concentration-and-solubility-of-h2>). Measurements were performed at pH 4.5 (50 mM K<sub>2</sub>HPO<sub>4</sub>/100 mM citric acid pH 4.5).

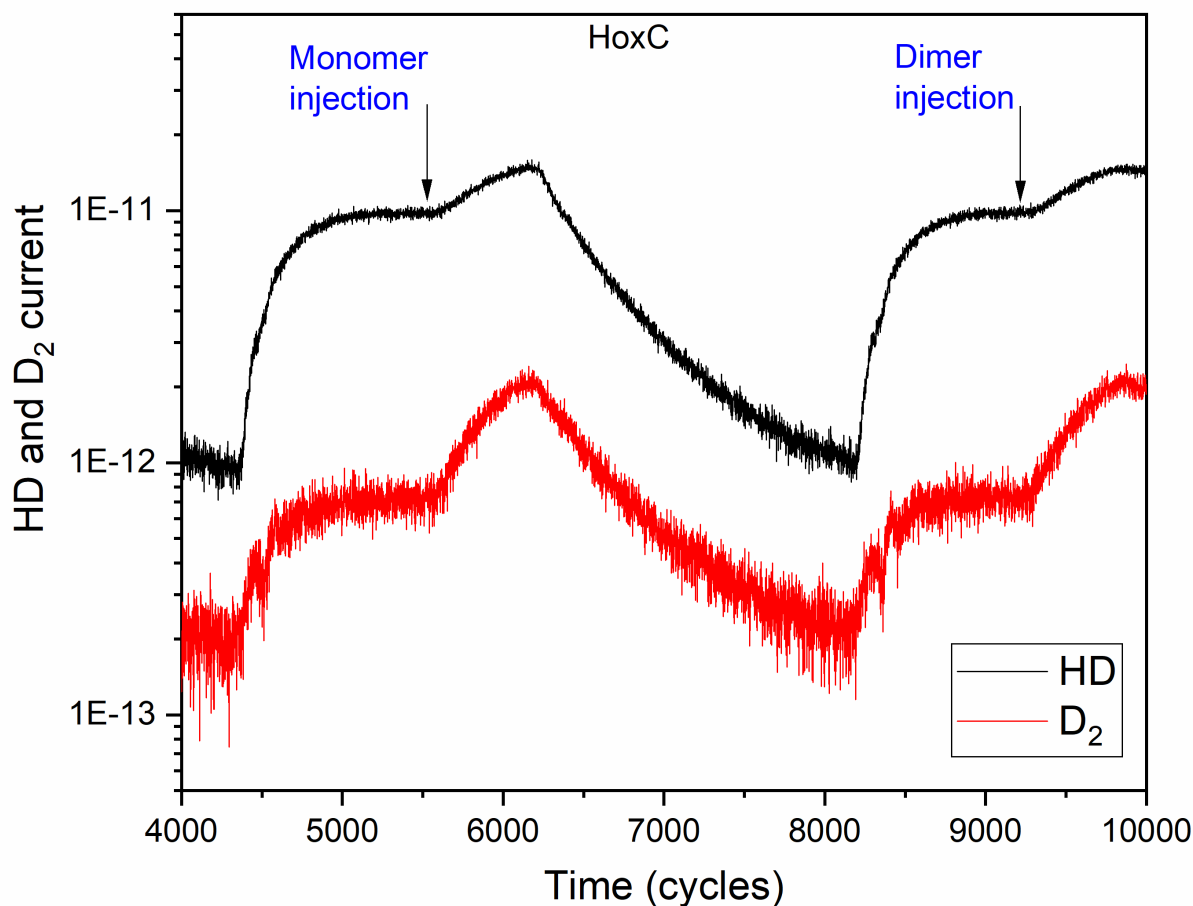


**Figure S18.** HD and D<sub>2</sub> current response of monomeric and dimeric HoxC as a function of the time. After stabilization of the HD and D<sub>2</sub> gas-derived currents under H<sub>2</sub>-saturating conditions, 10 μl of HoxC monomer and 10 μl of HoxC dimer (10-12 mg/ml) were injected into the reaction chamber. The mass spectrometer response to changing amounts of HD and D<sub>2</sub> gas was monitored. Measurements were performed at pH 4.5 in 50 mM K<sub>2</sub>HPO<sub>4</sub>/100 mM citric acid. No difference were detected between monomeric and dimeric protein (HD and D<sub>2</sub> production rates of  $0.78 \cdot 10^{-3} \text{ s}^{-1}/0.2 \cdot 10^{-3} \text{ s}^{-1}$  for HoxC monomer and  $0.76 \cdot 10^{-3} \text{ s}^{-1}/0.18 \cdot 10^{-3} \text{ s}^{-1}$  for HoxC dimer). The data are not corrected for the continuous decrease in gas concentration, which was caused by the vacuum pipeline connecting the measurement chamber with the detector of the mass spectrometer. 1 cycle took 0.8 s.

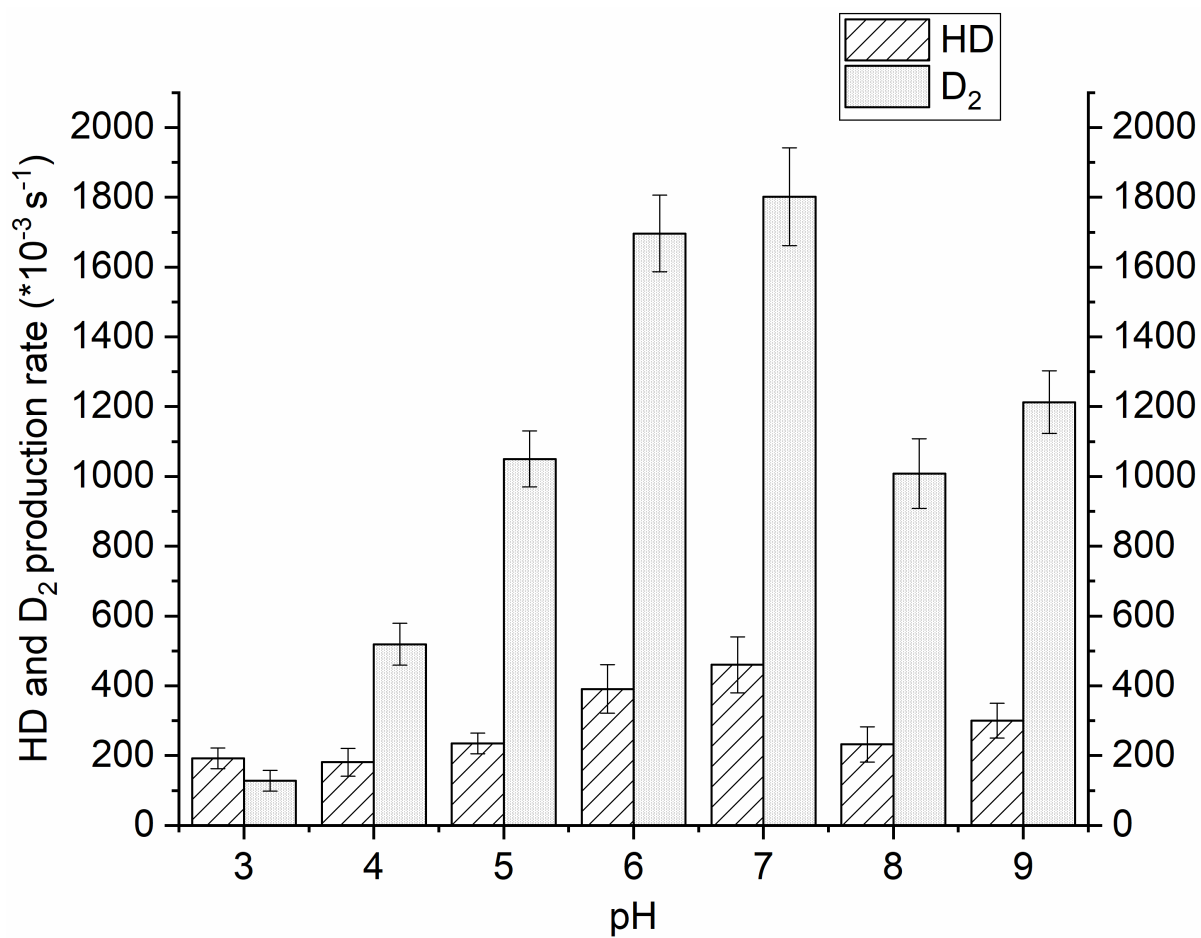


**Fig. S19.** HD and D<sub>2</sub> production rates of RH as a function of the pH. Highest activity was detected at pH 7.0 with a HD and D<sub>2</sub> production rate of  $460 \times 10^{-3} \text{ s}^{-1}$  and  $1802 \times 10^{-3} \text{ s}^{-1}$  respectively. Error bars indicate the standard deviation calculated from three independent measurements.

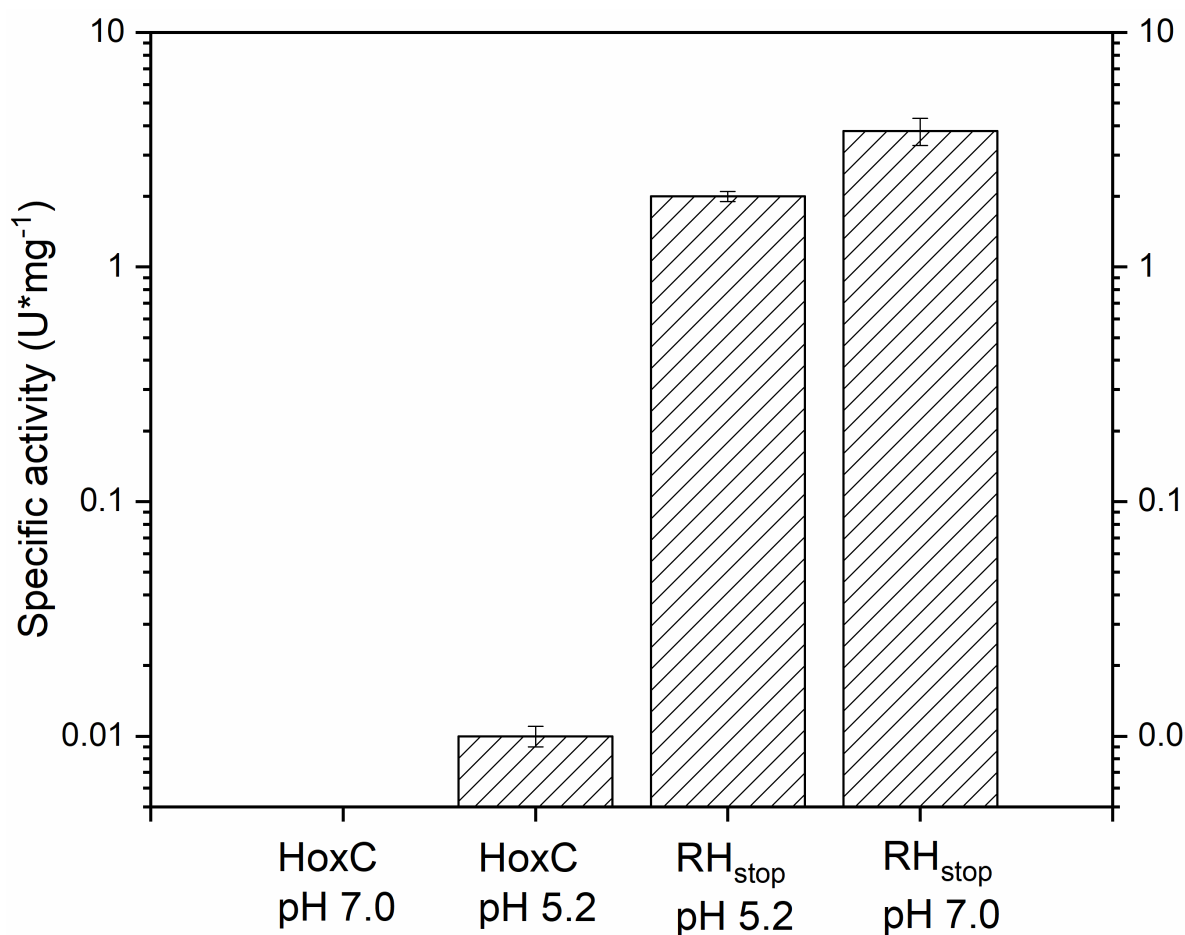


**Fig. S20.** H<sub>2</sub>-dependent methylene blue reduction mediated by HoxC and RH at different pH values. Error bars indicate the standard deviation calculated from four independent measurements. Note that the y-axis has a logarithmic scale.

**Table S8.** Comparison of HD/D<sub>2</sub> ratios at different HoxC concentrations

| HoxC amount | HD/D <sub>2</sub> * |
|-------------|---------------------|
| 50 μg       | 3.8                 |
| 100 μg      | 4.5                 |
| 200 μg      | 3.7                 |
| 300 μg      | 3.9                 |

\*The given HD/D<sub>2</sub> ratios represent the average of two independent measurements.

## Supplementary References

- 1 G. Winter, T. Buhrke, O. Lenz, A. K. Jones, M. Forgber and B. Friedrich, *FEBS Lett.*, 2005, **579**, 4292–4296.
- 2 S. Löscher, I. Zebger, L. K. Andersen, P. Hildebrandt, W. Meyer-Klaucke and M. Haumann, *FEBS Lett.*, 2005, **579**, 4287–4291.
- 3 O. Lenz, L. Lauterbach and S. Frielingsdorf, in *Methods in Enzymology*, Elsevier, 2018, vol. 613, pp. 117–151.
- 4 T. Buhrke, O. Lenz, N. Krauss and B. Friedrich, *J. Biol. Chem.*, 2005, **280**, 23791–23796.
- 5 T. Buhrke, S. Löscher, O. Lenz, E. Schlodder, I. Zebger, L. K. Andersen, P. Hildebrandt, W. Meyer-Klaucke, H. Dau, B. Friedrich and M. Haumann, *J. Biol. Chem.*, 2005, **280**, 19488–19495.
- 6 P. A. Ash, J. Liu, N. Coutard, N. Heidary, M. Horch, I. Gudim, T. Simler, I. Zebger, O. Lenz and K. A. Vincent, *J. Phys. Chem. B*, 2015, **119**, 13807–13815.
- 7 F. Roncaroli, E. Bill, B. Friedrich, O. Lenz, W. Lubitz and M.-E. Pandelia, *Chem. Sci.*, 2015, **6**, 4495–4507.
- 8 R. Breglia, C. Greco, P. Fantucci, L. De Gioia and M. Bruschi, *Inorg. Chem.*, 2019, **58**, 279–293.
- 9 T. Krämer, M. Kampa, W. Lubitz, M. van Gastel and F. Neese, *ChemBioChem*, 2013, **14**, 1898–1905.
- 10 B. Suo, K. Shen, Z. Li and W. Liu, *J. Phys. Chem. A*, 2017, **121**, 3929–3942.
- 11 S. Hartmann, S. Frielingsdorf, A. Ciaccafava, C. Lorent, J. Fritsch, E. Siebert, J. Priebe, M. Haumann, I. Zebger and O. Lenz, *Biochemistry*, 2018, **57**, 5339–5349.
- 12 I. Bürstel, E. Siebert, G. Winter, P. Hummel, I. Zebger, B. Friedrich and O. Lenz, *J. Biol. Chem.*, 2012, **287**, 38845–38853.
- 13 P. Vignais, *Coord. Chem. Rev.*, 2005, **249**, 1677–1690.